EFDA–JET–PR(08)30

I. Voitsekhovitch, B. Alper, M. Brix, R.V. Budny, P. Buratti, C.D. Challis,
J. Ferron, C. Giroud, E. Joffrin, L. Laborde, .T.C. Luce, D. McCune,
J. Menard, M. Murakami, J.M. Park and JET EFDA contributors

Non-inductive Current Drive and Transport in High β_N Plasmas in JET

Non-inductive Current Drive and Transport in High β_N Plasmas in JET

I. Voitsekhovitch[1], B. Alper[1], M. Brix[1], R.V. Budny[2], P. Buratti[3], C.D. Challis[1], J. Ferron[4], C. Giroud[1], E. Joffrin[5], L. Laborde[1], .T.C. Luce[4], D. McCune[2], J. Menard[2], M. Murakami[6], J.M. Park[6] and JET EFDA contributors*

JET-EFDA, Culham Science Centre, OX14 3DB, Abingdon, UK

[1]EURATOM-UKAEA Fusion Association, Culham Science Centre, OX14 3DB, Abingdon, OXON, UK
[2]Princeton Plasma Physics Laboratory, Princeton, New Jersey, 08543-0451, USA
[3]Associazione EURATOM/ENEA sulla Fusione, Frascati, Italy
[4]General Atomics, San Diego, California 92186-5608, USA
[5]Association Euratom CEA, CEA/DSM/IRFM, Cadarache, 13108 Saint-Paul-lez-Durance, France
[6]Oak Ridge National Laboratory, Oak Ridge, Tennessee 37831, USA
** See annex of F. Romanelli et al, "Overview of JET Results ",*
(Proc. 22[nd] IAEA Fusion Energy Conference, Geneva, Switzerland (2008)).

Preprint of Paper to be submitted for publication in
Nuclear Fusion

ABSTRACT.

A route to stationary MHD stable operation at high β_N has been explored at the Joint European Torus (JET) by optimising the current ramp up, heating start time and the waveform of Neutral Beam Injection (NBI) power. In these scenarios the current ramp up has been accompanied by plasma preheat (or the NBI has been started before the current flat top) and NBI power up to 22 MW has been applied during the current flat top. In the discharges considered transient total $\beta_N \approx 3.3$ and stationary (during high power phase) $\beta_N \approx 3$ have been achieved by applying the feedback control of β_N with the NBI power in configurations with monotonic or flat core safety factor profile and without an Internal Transport Barrier (ITB). The transport and current drive in this scenario is analysed here by using the TRANSP and ASTRA codes. The interpretative analysis performed with TRANSP shows that 50–70% of current is driven non-inductively; half of this current is due to the bootstrap current which has a broad profile since an ITB was deliberately avoided. The GLF23 transport model predicts the temperature profiles within a +/–22% discrepancy with the measurements over the explored parameter space. Predictive simulations with this model show that the $E \times B$ rotational shear plays an important role for thermal ion transport in this scenario, producing up to a 40% increase of the ion temperature. By applying transport and current drive models validated in self-consistent simulations of given reference scenarios in a wider parameter space, the requirements for fully non-inductive stationary operation at JET are estimated. It is shown that the strong stiffness of the temperature profiles predicted by the GLF23 model restricts the bootstrap current at larger heating power. In this situation full non-inductive operation without an ITB will strongly rely on the external non-inductive current drive sources.

I. INTRODUCTION

A route to the so-called "advanced tokamak scenario", i.e. stationary, MHD stable fully (or largely) non-inductive operation where the confinement is improved with respect to the ordinary H-mode confinement, has been investigated in a number of tokamaks [1 - 7]. Experimentally, advanced scenarios routinely take advantage of fast ohmic current ramp-up or/and plasma pre-heat during the current ramp up phase delaying the penetration of the ohmic current to the plasma core. The pre-heat phase is followed by high power heating applied close to the current flat-top where the non-inductive currents from the external sources in combination with the bootstrap current are supposed to replace the ohmic current fully, or partly, while maintaining an appropriate safety factor profile q (i.e., reversed q-profile or low shear in the core plasma region for the regimes with an Internal Transport Barrier (ITB) or monotonic profile with $q_0 > 1$ for sawtooth-free operation). In plasmas with a strong ITB obtained in configurations with reversed safety factor profile the maintenance of the stationary alignment of the non-inductive currents may be difficult because of the strong non-linear coupling of the pressure and current density profile due to the q-dependent transport coefficients and the pressure gradient dependent bootstrap current. The uncontrolled reduction of the reversed shear region with the subsequent degradation of the ITB in plasmas where the magnetic shear produces a strong stabilising effect on the anomalous thermal transport has been demonstrated in the predictive modelling of advanced scenarios

for Tore Supra [8] and ITER [9]. The importance of the simultaneous control of the current and pressure profiles in high performance plasmas with an ITB has stimulated the development of real-time current profile control algorithms (see for example, Ref. 10).

An alternative approach to advanced tokamak operation where a strongly localised bootstrap current density profile is avoided consists in the development of the thermal equilibria with a broad pressure profile and large edge pressure pedestal, but without an ITB. Such a scenario performed on DIII-D [2], JT-60U [4, 5] and ASDEX Upgrade [6] appears to be competitive with ITB discharges demonstrating a large normalised pressure $\beta_N = (aB_T/I_{pl})\beta_T(\%)$ (here a is the minor radius, B_T is the toroidal magnetic field, I_{pl} is the plasma current, β_T is the toroidal beta, $\beta_T = 2\mu_0 < p > / B_T^2$ and angular brackets mean the volume average), good confinement properties and long duration (few resistive times). This scenario has been performed in a broad q_{95} range ($q_{95} = 3.2 - 5$ [2, 6, 7]) and at densities up to $0.8 n_{Gr}$ ($n_{Gr} = I_{pl}/\pi a^2$ is the Greenwald density with units of 10^{20} m^{-3}, a is minor radius in meters and the plasma current is in MA) with the $H_{IPB98(y,2)}$ factor increasing up to 1.5 [6] (here $H_{IPB98(y,2)} = \tau_E / \tau_{IPB98(y,2)}$, τ_E is the thermal energy confinement time, $\tau_{IPB98(y,2)}$ is defined in Ref. 11). This kind of advanced operation is characterised by a monotonic or flat core q-profile with $q_0 > 1$ that prevents the sawtooth oscillations. A modest $m = 3/n = 2$ (m is the poloidal mode number and n is the toroidal mode number) tearing mode is sometimes observed in this scenario [2, 5], and in some cases this mode appears to be responsible for the broadening of the current profile and maintaining $q_0 \geq 1$ [2]. The stationary β_N value maintained for few resistive times during the high heating power phase varies in the range 2.5 – 3.4 in different tokamaks, somewhat exceeding the no-wall limit in some cases [2 - 5]. Non-inductive current drive close to 100% has been achieved in this scenario [3].

Recently, similar experiments aimed at largely non-inductive operation in MHD stable conditions at high β_N have been performed in the Joint European Torus (JET) [12, 13]. In the discharges considered high β_N values (up to 3.3 transiently and up to 3 in stationary conditions) have been achieved in the Neutral Beam Injection (NBI) heated discharges by applying feedback control of β_N with NBI power in a high triangularity magnetic configuration, at low magnetic field and plasma current. The optimisation of this scenario has been studied by varying the current ramp rate dI_{pl}/dt and applying the ICRH and NBI pre-heat during the current ramp up. The start time of the low power NBI preheat t_{NBI} and the NBI power waveform have been varied as well. This paper presents the transport and current drive analysis of 26 discharges covering the operational parameter space $t_{NBI} = 1.5 - 4$s, $P_{NBI} = 9 - 22$MW and the current ramp rate $dI_{pl}/dt = 0.12 - 0.73$MA/s (determined during the 30% rise of plasma current before the flat top). The goals of this analysis are the calculation of the non-inductive currents and their alignment in the high heating power phase, the identification of the most important contributions to the bootstrap current, the modelling of the current profile evolution and identification of the transport model which gives a reasonable prediction of the observed temperature evolution. The code simulations play an important role in this study as a tool for: the estimation of the key parameters in these scenarios; testing data consistency; providing validation of the transport model; and the projection of the experimental scenario to a larger parameter space. The analysis of the current

profile evolution along with the data consistency analysis is performed here with the TRANSP code [14]. The ASTRA code [15] is used for the self-consistent predictive modelling of experimental scenario including the modelling of thermal transport, current profile evolution and NBI physics. By applying the transport and current drive models validated in the self-consistent simulations of reference experimental scenarios to a wider parameter space the requirements for a fully non-inductive stationary operation at JET are determined.

This paper is organised as follows. The experimental scenario will be briefly described in Section II. In Section III, the analysis of the non-inductive current drive and the q-profile evolution in this scenario as performed with the TRANSP code will be presented. The validation of the GLF23 model [16] in the discharges performed in the parameter space described above and the self-consistent modelling of the reference scenario with a long NBI heating phase is given in Section IV. This Section also presents the simulations aimed at the optimisation of the reference scenario by raising the NBI power, applying the strong electron heating and varying the density and density profile. The results of the interpretative analysis and predictive modelling of high β_N scenario are summarized and discussed in Section V.

2. EXPERIMENTAL SCENARIO WITH HIGH β_N

A high β_N scenario without an ITB has been developed at JET in a high triangularity magnetic configuration ($\delta < 0.43$), at relatively low magnetic field B_T = 1.8T and plasma current I_{pl} = 1.2MA ($q_{95} \approx 5$). A low power NBI preheat has been applied during the current ramp up in some discharges to delay the inward penetration of the plasma current. An early and low power ICRH preheat ($P_{ICRH} < 2$ MW) has been also used in few discharges. The L-H transition occurs soon after the start of the NBI heating. The deuterium gas puff applied during the current ramp up was switched off at the beginning of the neutral beam injection to prevent the degradation of the pedestal pressure. The value of b_N was controlled by feedback on the NBI power. A broad range of the key parameters governing the evolution of the current density profile and plasma pressure has been explored during the scenario development. In particular, the rate of the current ramp from 0.8 to 1.2MA, the start time of the NBI heating and the NBI power at current flat-top have been varied in the range dI_{pl}/dt = 0.12–0.73MA/s, t_{NBI} = 1.5–4s and P_{NBI} = 9–22MW. As a result of the optimisation of these parameters b_N up to 3.3 has been achieved for the discharges considered. This increase occurs due to the increase of the electron and ion temperature, density and density peaking which vary in the range T_{e0} = 3–6.5keV, T_{i0} = 3.5–8.5keV, n_{e0} = (2.9 - 4.6)10^{19} m^{-3}, $n_{e0}/\langle n_e \rangle$ = 1.2–1.6 (here the subscript 0 stands for the central value and $\langle n_e \rangle$ is the volume averaged density). The plasma profiles obtained in this scenario do not display strong ITBs, although weak and short-lived ITBs appeared occasionally. The sawtooth oscillations have not been observed in the analysed discharges, indicating that the central safety factor was sustained above one. An n = 1 mode was frequently observed at high power and early NBI start time. Of the 26 discharges analysed 12 discharges had an n = 1 mode, but the phase once the n = 1 mode had commenced was not considered for the plasma performance and

statistical analysis described later (see Sections III and IV).

Typical high β_N scenario discharges are illustrated on Fig. 1, which shows the evolution of plasma current, NBI power, line averaged density, β_N and the amplitude of the $n = 1$ mode. The discharges shown in this figure are characterised by different NBI start times and heating powers at the current flat top. ICRH preheat during the current ramp up has been applied in one of these discharges (Pulse No: 68767). The $n = 1$ mode has been observed from around 4.5 s in the discharge with early ICRH preheat and high NBI power (22 MW, Pulse No: 68767) while the discharge with early NBI preheat and lower heating power (Pulse No: 70207) and the discharge with high NBI power and later NBI start (Pulse No: 68875) do not exhibit this MHD activity. The detrimental effect of the $n = 1$ mode is illustrated by Fig.1d showing that the β_N value drops by 25% with the onset of this mode in discharge Pulse No: 68767 down to the value obtained in a discharge with half the NBI power (see also Ref. 17).

The following diagnostics have been used for the profile measurements. The electron temperature and density have been measured using Thomson scattering diagnostics with a spatial resolution of 5cm and time resolution of 250ms. A twelve channel Charge-eXchange (CX) diagnostics with a 10ms time resolution has been used for the measurements of ion temperature, toroidal rotation of carbon impurity and effective charge Z_{eff} in the outer half of plasma column. The q-profile has been reconstructed in the EFIT [18] simulations constrained by the thermal pressure estimated with the measured density and temperature profiles, fast ion pressure calculated with the PENCIL code [19], polarimetry from the FIR interferometer and Motional Stark Effect (MSE) measurements. Finally, the TRANSP code has been used for the validation of the consistency of kinetic and magnetic measurements.

3. *Q*-PROFILE EVOLUTION AND NON-INDUCTIVE CURRENT DRIVE

Three different tools have been used to obtain information about the evolution of the q-profile: (i) the observation of Alfvén cascades [20], (ii) EFIT simulations with the constraints mentioned in Section II and (iii) TRANSP simulations. The Alfvén cascades have been typically observed in this scenario during the current ramp up in ohmic plasma and early NBI preheat. They were not registered later on during the high power heating phase except in the discharge with the earliest NBI start time $t_{NBI} = 1.5$s (Pulse No: 68780). In the latter discharge the Alfvén cascades have been clearly observed during the whole NBI heating phase apart from a short time interval (0.9s) when a strong $n = 1$ mode is present. The observation of the Alfvén cascades confirms that a reversed q-profile has been formed during the current ramp up phase and maintained till the high NBI heating in many discharges.

The simulations of the current profile diffusion with TRANSP have been performed with the measured plasma profiles (see Section II) for the whole NBI heating phase starting with the ohmic plasma just before the NBI. The NCLASS module [21] has been used for computing the plasma resistivity and bootstrap current I_{BS}. The beam driven current I_{NBI} has been simulated with the Monte-Carlo NUBEAM module [22] in TRANSP, which integrates the guiding centre drift orbit equation for fast ions taking into account their orbit losses and classical diffusion. The TRANSP simulations of the

ohmic phase have been performed with the prescribed q-profile taken from the EFIT reconstruction constrained by the magnetic probe measurements only, since the measurements of the ion temperature and MSE data are not available in ohmic plasmas. The transition from this initial profile to the q-profile simulated with the poloidal field diffusion equation has been performed a few hundred milliseconds before the NBI heating. With this choice of the start time for the current diffusion equation a reasonable agreement of the time-evolving q-profile simulated with TRANSP and reconstructed with EFIT, including MSE constraints, has been obtained during the NBI heating phase for the majority of discharges. Such a relatively late start for the diffusion equation was also chosen because of the relatively low signal to noise ratio of the Thomson scattering data during the early ohmic phase of the discharge.

The evolution of the central safety factor in the 26 analysed discharges as obtained with EFIT and TRANSP is summarised by two extreme cases in Fig.2 (top panel). The curves in this figure show the q_0 evolution simulated with TRANSP in discharges with the early and late NBI preheat (Pulse No: 70207, $t_{NBI} = 2.3$s and Pulse No: 70254, $t_{NBI} = 3.5$s). The symbols show the q_0 evolution reconstructed with EFIT using MSE data for the same discharges. These two discharges represent the case where the most efficient delay in the current penetration has been achieved with early heating (Pulse No: 70207) and, at the opposite extreme, a case with late NBI heating (Pulse No: 0254). The time traces of the q_0 during the NBI heating phase for other discharges are located within the region limited by the solid and dashed curves. The fast drop of the q_0 during the first 3s obtained with TRANSP is typical for all discharges. A weakly reversed q-profile, similar to the profile shown by the solid curve on the bottom panel of Fig.2, has been obtained at this phase. The existence of the reversed q-profile at this phase is confirmed by the observation of Alfvén cascades mentioned above. Further evolution of the q-profile depends on the heating scenario. The reduction of q_0 is usually delayed in discharges with the ICRH preheat (the ICRH preheat starts typically at 1.5s and lasts for 0.5−2.5s), larger current ramp rate and high NBI heating, while the q_0 value decreases to one soon after the start of NBI in discharges with late heating as shown on the top panel of Fig.2. But independent of the delay in the q_0 relaxation at the beginning of the NBI heating, the safety factor profile always evolves toward a monotonic shape with the central q value slightly above one in discharges with a long duration NBI phase. The typical monotonic q-profile obtained at the end of this long high power phase is shown in Fig.2 (dashed curve on the bottom panel). This q-profile is in a good agreement with the EFIT reconstruction for the same discharge (Pulse No: 70254), but the position of the $q = 3/2$ surface is more off-axis (around $R = 3.45$m) than the location of the $m/n = 3/2$ mode (around $R = 3.3$m) obtained with ECE measurements of the mode, tending to point to underestimate q-values in the central region of around $\rho = 0.2$ to 0.3 (r is the square root of normalised toroidal flux) in the TRANSP simulations. It should be mentioned that the agreement in the simulated q profile between TRANSP and EFIT (Fig.2) is achieved only for discharges with $t_{NBI} \geq 2.3$s while a disagreement has been found for the discharge with early ICRH and NBI pre-heat and large current ramp rate (Pulse No: 68780, Fig.2, middle panel). In the Pulse No: 68780 the weakly reversed q-profile has been maintained till the end

of the NBI heating in TRANSP simulations while the EFIT reconstruction indicates a reduction of the q_0 during the onset of strong $n = 1$ mode. This mode has been accompanied by the accumulation of light impurities in the core, but the increase of resistive time due to impurity accumulation is taken into account in TRANSP and does not explain such a fast reduction of q_0. This discharge gives an interesting example of a non-classical evolution of the current profile in the presence of strong MHD activity (an effect not included in the TRANSP modelling) and the understanding of this evolution is still an open issue. It should also be mentioned that the discrepancy between q-profiles reconstructed with EFIT and simulated with different codes using the neoclassical models for the bootstrap current and current conductivity has been found also in the DIII-D discharges during the current ramp up phase [23].

The q-profile obtained in TRANSP simulations, matching the q-profile reconstructed with EFIT, has been used in further analysis of the discharges with $t_{NBI} > 2.3$s. The analysis of the discharge with early NBI preheat shown in Fig.2 (middle panel) has been performed by using the q-profile reconstructed with EFIT.

One of the objectives of the analysed scenario is the achievement of the high normalised thermal pressure, since this parameter determines the bootstrap current and fusion performance. The feedback control used in these discharges provides the control of the total β_N which includes the contribution of thermal and fast ion pressure. The contribution of the normalised thermal pressure $\beta_{N,thermal}$ and the fast ion pressure $\beta_{N,fast}$ to the total β_N obtained in the explored parameter space is shown in Figure 3. The thermal normalised pressure has been calculated with TRANSP by using the measured electron and ion temperature, electron density and Z_{eff} profiles. The ion density is calculated by using the quasi-neutrality equation. The fast ion normalised pressure is calculated using the NUBEAM module in TRANSP. Both thermal and fast ion pressure increase with β_N. The ratio of thermal to total β_N varies between 0.6 and 0.8 over the performed parameter scans showing no trend with the total β_N or NBI power.

The thermal pressure includes the contributions from the core and the pedestal. These two contributions are shown in Figure 4. The analysed discharges are characterised by the type I Edge Localised Modes (ELMs) and high pedestal pressure (here we use the plasma pressure estimated by TRANSP at $\rho = 0.8$, i.e. at the outmost CX data point, to characterise the pedestal). A high pedestal pressure has already been achieved in a discharge with relatively low total β_N (~ 1.7) and it increases by a factor 2 in the explored parameter space. This increase occurs due to the increase of both electron and ion pedestal pressure. The central thermal pressure P_0 increases slightly faster than the pedestal pressure $P(\rho = 0.8)$ (the difference $P_0 - P(\rho = 0.8)$ is increased by factor 2.5) and this increase occurs mainly due to the increase of the core ion temperature.

The non-inductive current consists of the bootstrap current and beam driven current. The fraction of these currents is plotted in Fig.5 (top). This figure shows also the fraction of the total non-inductive current. The fraction of each non-inductive current is plotted as function of the β_N of the species driving this current, i.e. the bootstrap current is plotted as a function of the thermal $\beta_{N,thermal}$ (note that

TRANSP does not calculate the bootstrap current due to fast ions), the beam driven current is plotted as a function of the fast ion $\beta_{N,fast}$ and the total non-inductive current is plotted as a function of the total β_N. The horizontal axis on this figure corresponds to the β_N values for different species while the light grey, dark grey and black lines show the range of the achieved fast ion, thermal and total β_N. As mentioned above the bootstrap current is calculated by using the NCLASS module in TRANSP for all analysed discharges. These calculations were cross-checked with the Sauter model [24] for a limited set of discharges and the obtained bootstrap and total current fractions are shown by stars in Fig.5. Generally, a slightly larger bootstrap current has been obtained with the Sauter model in the explored parameter space characterised by a volume averaged $<Z_{eff}> = 1.3-1.8$ and averaged collisionality at mid-radius $<\nu_e^*(r/a=0.5)> = 0.03$ - 0.07. The simulations show that values of non-inductive current up to 0.9 MA (75% of the total current) have been achieved at largest β_N, however, at these largest β_N, this non-inductive current is obtained transiently before the onset of the $n = 1$ mode. The reduction of the plasma pressure caused by this mode leads to the reduction of the bootstrap current and total non-inductive current. In moderately heated (15–17MW) MHD stable discharges the relatively stationary non-inductive current fraction was 63%. Generally, half of the non-inductive current is driven by the bootstrap current. Typical bootstrap and beam driven current density profiles obtained in a high β_N discharge are shown on Fig.5 (bottom). The beam driven current is slightly off-axis while a broad bootstrap current density profile has been achieved in the majority of discharges due to the broad pressure profiles (and the absence of an ITB).

The bootstrap current is driven by the gradient of density ($I_{BS}^{\nabla n}$) and gradients of ion ($I_{BS}^{\nabla Ti}$) and electron ($I_{BS}^{\nabla Te}$) temperature. To identify the main contribution to the bootstrap current at $\rho \leq 0.8$ (i.e., excluding the edge bootstrap current since high resolution profile measurements are not available for the whole database) the currents driven by the gradients of various quantities have been calculated separately by using the Sauter model in TRANSP. The results of these calculations are shown in the $I_{BS}^{\nabla T} - I_{BS}^{\nabla n}$ parameter space (Fig. 6). The dashed line in this figure separates the regions with $I_{BS}^{\nabla T} > I_{BS}^{\nabla n}$ (above the dashed line) and $I_{BS}^{\nabla T} < I_{BS}^{\nabla n}$ (below the dashed line). The symbols show the $I_{BS}^{\nabla Ti}$ (closed squares) and $I_{BS}^{\nabla Te}$ (open circles) terms plotted as a function of the $I_{BS}^{\nabla n}$ term for each discharge. The largest contribution to the bootstrap current comes from the gradient of electron temperature in the majority of discharges. The part of the bootstrap current driven by the ion temperature gradient is generally lower than the ∇T_e and ∇n driven terms. The majority of the discharges display a relatively low density peaking factor explaining the modest contribution of the density gradient term to the total bootstrap current. The density gradient produces the largest contribution to the bootstrap current only in the discharge with the largest density peaking ($n_{e0} / <n_e> \approx 1.62$, Pulse No: 68876).

Since the ∇T_e–driven bootstrap current is generally larger than the other contributions the possibility to raise the bootstrap current by increasing the electron temperature has been investigated. The beam driven current could also benefit from an increase of electron temperature due to the temperature dependent current drive efficiency [25] determined by the slowing down time of the NBI fast ions. To estimate the effect of the electron temperature profile on the non-inductive currents in these experiments

the electron temperature in Pulse No's: 69001 (I_{BS} = 0.45MA with dominant ∇T_e–contribution) and 68876 (I_{BS} = 0.43MA with dominant ∇n contribution) has been artificially re-scaled at $\rho \leq 0.5$ by a factor varying from 1.5 to 3 starting from 4.2 keV and 4.6 keV correspondingly. Then the equilibrium, current profile diffusion and NBI have been simulated with TRANSP for the two discharges taking a re-scaled electron temperature along with other measured data used in interpretative TRANSP simulations (see Section II for plasma profiles). It has been found that full non-inductive current drive is achieved at T_{e0} = 13keV in discharge # 68876 due to the equally increased bootstrap and beam driven currents. Each non-inductive current mechanism drives about 50% of the total plasma current in this case. The non-inductive current fraction in Pulse No: 69001 was still 83% when the temperature was increased by a factor 3. Such a temperature increase from 4.6keV (as it is in discharge 68876) to 13keV would probably require the formation of a thermal electron ITB or operation at high ICRH power in addition to NBI heating.

Other predictive simulations have been performed with TRANSP to find out whether a stationary q-profile with $q_0 > 1$ can be achieved with the experimental density, temperature and Z_{eff} profiles under the assumption of unlimited NBI duration. The data in the interpretative TRANSP runs for a few discharges (including the NBI power) have been frozen at a given time and the current diffusion and plasma equilibrium only have been simulated for a further time interval of 1 minute. The stationary configuration with radially flat toroidal voltage profile (the radial variation of the toroidal voltage was less than 0.45%) has been achieved within this time interval. Generally, the important parameters determining the q-profile in stationary conditions are the magnitude and the radial profile of the non-inductive currents and the current conductivity profile. The classical current conductivity σ depends on the profile of Z_{eff} and the electron temperature, $\sigma \propto T_e^{3/2}/Z_{eff}$. The profile of Z_{eff} does not exhibit a strong variation from shot to shot showing the same slightly off-axis peaking. The peaking of the electron temperature profile $T_{e0}/\langle T_e \rangle$ varies between 1.6 and 2.5 in different discharges with the low value obtained either in discharges with a high T_e pedestal or after the onset of an $n = 1$ mode when the reduction of the central electron temperature is larger than the reduction of the pedestal temperature. The stationary equilibrium has been simulated for discharges with electron temperature peaking varying between 1.6 and 2.4, different magnitudes of non-inductive currents and different fractions of edge bootstrap current. The profiles of the beam driven and bootstrap currents are similar in all discharges used for the stationary simulations (see Fig. 5, bottom panel).

Figure 7 shows the comparison of two stationary equilibria based on the plasma profiles at 5.5 and 6s in Pulse No: 68876. The density profile is nearly the same at these times while the electron temperature profile is slightly broader, and the ion temperature profile is steeper at 6s (Fig.7, top). The higher T_e pedestal and steeper T_i profile at 6s lead to a slight increase in the core and edge bootstrap current and, therefore, to the reduction of the ohmic current (Fig.7, middle panel). In addition, the broadening of the electron temperature profile contributes to the broadening of the remaining ohmic current density profile at 6 s ($j_{OH} \sim T_e(r)^{3/2}E$, the parallel electric field E is constant along the radius at the end of simulations). As a result the minimum safety factor is slightly above one in the stationary

equilibrium based on the plasma profiles taken at 6 s while the stationary configuration based on the plasma state at 5.5s would have $q_0 < 1$ (Fig.7, bottom). The safety factor profile obtained in TRANSP at 5.5–6s is also shown on Fig.7 (bottom) for comparison with the stationary profiles.

The predictive simulations of the stationary equilibria based on the eight experimentally obtained plasma states are summarised in Fig. 8 where the minimum safety factor (which is equal to the central safety factor for the majority of simulated equilibria) is plotted as a function of electron temperature peaking. The fraction of the total non-inductive current is indicated for each discharge. The NBI power varies in the range 10–22MW for the selected plasma states resulting in different beam driven currents. The simulations show that the steady-state solution with q_0 (or q_{min}) above one has been achieved in the MHD stable Pulse No: 70199 with a broad T_e profile, moderate NBI power (15MW) and fraction of the non-inductive current (56%), and in Pulse No: 68876 (Fig.7). The q_0 value is below one in the stationary configurations with more peaked electron temperature in spite of an even larger non-inductive current obtained in some cases. The difference in the edge bootstrap current in discharges with the same electron temperature peaking factor also contributes to the scatter of the data points.

These predictive simulations show that sawtooth-free stationary magnetic equilibria can be obtained with the experimentally achieved pressure profiles by extending the NBI duration, but these equilibria are very sensitive to the electron temperature peaking.

4. PREDICTIVE MODELLING

The analysis performed in the previous section shows that the stationary q_0 value is sensitive to the electron temperature profile. Comparable $I_{BS}{}^{\nabla Ti}$ and $I_{BS}{}^{\nabla Te}$ terms obtained for some discharges (see Fig.6) suggests also that the ion temperature profile may produce an important contribution to the total and local bootstrap current. In such a situation the estimation of the non-inductive and steady-state capabilities of the high β_N scenario, and its possible optimisation, would benefit from self-consistent transport and current diffusion modelling. The choice of an appropriate transport model is an important issue for predictive transport modelling. In this section the predictive modelling of experimental scenarios is performed in two steps. First, the GLF23 model is validated in simulations of the electron and ion temperature evolution in 12 high β_N discharges which have different q profiles and heating power. Other plasma parameters have been prescribed in these simulations. Second, self-consistent transport, current diffusion and NBI modelling of the experimental scenario have been performed. Based on the results, the high β_N plasmas have been projected to a different parameter space, including higher plasma density, NBI power and electron heating. The predictive modelling has been performed with the ASTRA code [15].

4.1. TEST OF THE GLF23 TRANSPORT MODEL

The theory-based GLF23 model which includes the Ion Temperature Gradient (ITG), Trapped Electron Mode (TEM) and Electron Temperature Gradient (ETG) driven transport has been tested against a

representative set of discharges. The selected discharges cover the whole explored range of NBI start time and power, and include also the plasmas with ICRH preheat. The electron and ion temperature have been simulated assuming the measured carbon toroidal rotation, Z_{eff} and electron density. The time evolving q-profile, NBI and ICRH heating sources, and sinks caused by the atomic processes have been calculated by TRANSP. The simulation of each discharge starts at the ohmic or ICRH heating phase just before the neutral beam injection and continues till the end of the NBI phase. Then the time interval $t_1 \leq t \leq t_N$ with the available CX measurements (the CX diagnostic beam was typically injected few hundreds milliseconds after the start of the NBI heating) has been selected for the estimation of prediction accuracy for the time evolving temperature profiles. In the MHD stable discharges this time interval includes nearly the whole NBI heating phase. In discharges with strong MHD activity the time interval starting from the beginning of the CX measurements (t_1) until the onset of an $n = 1$ mode (t_N) has been used for the estimation of the deviation from the model prediction. Thus, the capability of the GLF23 model to predict thermal transport has been estimated for the MHD stable phases of the discharges with evolving NBI heating power and q-profile. The simulations of the MHD unstable plasmas performed until the end of the NBI heating phase show that the temperatures are strongly over-predicted after the onset of an $n = 1$ mode.

The standard expressions for the estimation of the rms deviation and offset for predicted temperatures have been used

$$rms = \left[\frac{1}{N+M} \sum_{t_n = t_1}^{t_N} \sum_{x_m = 0}^{x_m = 0.7} \frac{\{T_{exp}(t_n, \rho_m) - T_{sim}(t_n, \rho_m)\}^2}{T_{exp}(t_n, \rho_m)^2} \right]^{1/2}$$

$$offset = \frac{1}{N+M} \sum_{t_n = t_1}^{t_N} \sum_{x_m = 0}^{x_m = 0.7} \frac{T_{exp}(t_n, \rho_m) - T_{sim}(t_n, \rho_m)}{T_{exp}(t_n, \rho_m)}$$

Here t_1 is the start time of the CX measurements, t_N is the end of the NBI heating phase for the MHD stable discharges or the time of the onset of an $n = 1$ mode, T_{exp} and T_{sim} stand for the experimental and simulated temperatures respectively, $N = (t_N - t_1)/\Delta t_{output}$ is the number of the time slices, $\Delta t_{output} = 0.1$ s is the output time interval, M is the number of radial points in the interval $0 \leq \rho_m \leq 0.7$. The fit quality is measured to $\rho_m = 0.7$ because shifted boundary conditions for electron and ion temperature $T_{sim}(\rho \geq 0.8) = T_{exp}$ have been used in all simulations, consistent with the radial location of the most outward point of the CX measurements being around $\rho = 0.8$.

The results of the validation of the GLF23 model for 12 discharges, summarised in Fig. 9, show that its predictive accuracy is within a +/−22% for both the electron and ion temperature. Since this estimate has been done in the evolving plasmas over a long time interval it includes also some data noise (the error bars for the T_i measurements are typically within 2% [26], large noisy bursts of T_e have been excluded from the Thomson scattering data). The simulations show that the ion temperature is well-predicted in the region $0.3 < \rho \leq 0.7$ for all discharges (two examples are shown in Fig.10) while the discrepancy with measured profiles was obtained in the plasma core in a few shots. In

discharges with late NBI start ($t_{NBI} \geq 2.5$ s) the core ion temperature tends to be over-predicted while the GLF23 model under-predicts the weak ITB in the discharge with $t_{NBI} = 2.3$s and larger central safety factor (Pulse No: 70207) that affects the time integrated discrepancy. Good agreement between the simulated and measured T_i profiles is restored in this discharge after the degradation of this ITB. The predictive accuracy of the GLF23 model for electron temperature in the confinement zone is lower than for the ion temperature. The electron temperature is under-predicted in the gradient region and the measured electron temperature profiles are found to be broader than the simulated profiles. It should be mentioned that in all simulated discharges the ITG driven turbulence is the dominant instability.

The temperature profiles obtained in the discharge with low NBI power and plasma density (Pulse No: 70200, $P_{NBI} = 10$MW, $n_{e0} = 2.8\times10^{19}$ m^{-3}) and high NBI power and plasma density (Pulse No: 68875, $P_{NBI} = 19$ MW, $n_{e0} = 3.4\times10^{19}$ m^{-3}) are shown in Fig.10. The simulation results presented on this figure have been obtained in a slightly different way than the results shown in figure 9. Here the profiles of the densities of thermal species, toroidal rotation, safety factor and NBI heating profiles have been frozen at a certain time and the simulations of electron and ion temperature have been performed with these profiles for the time duration of 4 s to assure the convergence of the simulations. Such simulations have been carried out with the GLF23 model both in ASTRA and TRANSP. It was found that the simulated ion temperature obtained with ASTRA and TRANSP is in a good agreement. A difference in electron temperature up to 9% in the core has been found. The reason for this difference is under investigation. Also very good agreement between the simulated and measured ion temperature has been obtained for both discharges while the prediction for electron temperature is less accurate. It should be mentioned that the temperature profiles obtained in the time evolving scenario (Fig.9) at the same times are similar to the profiles shown on Fig.10.

Figure 10 illustrates also the effect of the $E\times B$ rotation shear in the simulated discharges. The $E\times B$ rotation shear has been estimated with the radial ion force balance equation by taking the deuterium toroidal rotation calculated with the measured carbon rotation, neoclassical poloidal rotation and pressure of the deuterium species (though it should be noted that there is some evidence that the poloidal rotation can exceed neo-classical values in other JET scenarios [27]). It was found that the main contribution to the $E\times B$ shear is produced by the sheared toroidal rotation. In the simulations shown on Figs.9 and 10 this value of the $E\times B$ rotation shear has been used without the adjustment coefficient in the GLF23 model (i.e. $\alpha_e = 1$, see Ref. 28 for the definition of α_e). To illustrate the effect of the $E\times B$ rotation shear on thermal transport simulations with the GLF23 model where the $E\times B$ shear was switched off ($\alpha_e = 0$) have been performed for the same discharges. A much lower ion temperature has been obtained in these simulations (thin dashed and solid curves in Fig.10) illustrating that an important increase of the ion temperature (up to 40%) is provided by the stabilising effect of the $E\times B$ rotation shear on thermal ion transport. However, the $E\times B$ shear estimated as described above is not sufficiently large to produce a weak ITB obtained in the discharge with earliest NBI start time and largest q_0 value discussed above. A strong increase of the $E\times B$ shear ($\alpha_e = 3$) is needed to

cause a weak ITB in this discharge. However, such a large shear value would be inconsistent with the results of the simulations for the other discharges, leading to a strong overestimation of T_i. The effect of the $E \times B$ shear on thermal electron transport in these simulations is relatively small.

4.2. SELF-CONSISTENT MODELLING OF THERMAL TRANSPORT AND CURRENT DIFFUSION IN AN EXTENDED PARAMETER SPACE

As a next step the self-consistent modelling of transport, current diffusion and NBI has been performed for the stationary plasma with a long NBI heating phase (Pulse No: 70199). After testing for self-consistency in simulations of this discharge the model has been used to project the plasma performance in an extended parameter space with a goal of optimising this scenario towards fully non-inductive operation with $q_0 > 1$.

The modelling of Pulse No: 70199 with the ASTRA code has been performed with prescribed deuterium n_d and impurity n_{imp} densities calculated in the interpretative TRANSP simulations, where the measured electron density and Z_{eff} profiles had been used. The NBI simulations are performed by using the 1D Fokker-Planck NBI package in ASTRA, which calculates the heating power deposited on electrons and ions, torque, beam driven current, perpendicular and parallel pressure of fast ions (the fast ion pressure is taken into account in the simulations of plasma equilibrium) and beam density n_{beam} [29]. Then the electron density n_e has been estimated in ASTRA from the quasi-neutrality equation, $n_e = n_d + Z_{imp} n_{imp} + n_{beam}$ (only carbon impurities are assumed). The NCLASS module in ASTRA has been used for the estimation of the neoclassical thermal electron and ion diffusivity, bootstrap current and current conductivity. The total thermal diffusivity for electrons and ions includes the sum of the neoclassical transport and anomalous transport estimated with the GLF23 model. The whole discharge starting from the ohmic phase until the end of the NBI heating has been simulated.

The evolution of electron and ion temperature at the plasma centre and mid-radius and central safety factor obtained in the simulations with measured toroidal rotation velocity are shown in Fig.11 (solid curves). A satisfactory agreement between the simulated and measured temperatures is obtained over a long period starting from the beginning of the NBI heating. The central ion temperature tends to be overestimated in the region $\rho < 0.15$ after 7.8s due to the stabilisation of drift modes in the plasma core. Outside this region a good predictive accuracy for the ion temperature, similar to the one shown on Fig.10, has been obtained. The simulated electron temperature profile is more peaked than the measured profile between 6 and 8.5s (the central T_e is overestimated while the T_e at mid-radius in underestimated). As shown in Section III the central safety factor in steady state is sensitive to the peaking of the electron temperature profile (Fig.8), therefore an overestimation of electron temperature peaking obtained in Pulse No: 70199 may affect the simulated q-profile. To check the sensitivity of the q-profile evolution to the T_e peaking, the modelling of the ion energy balance, current diffusion and NBI for Pulse No: 70199 has been repeated taking into account the measured electron temperature profile. The results of these simulations are added to Fig.11 (dashed curves on the middle and bottom panel). Better agreement between simulated and measured ion temperature after 8s has been obtained

in this case. Although the q_0 values obtained with the simulated electron temperature are in a good agreement with the EFIT reconstruction (Fig.11, bottom, solid curve and symbols), the absence of the sawtooth oscillations in this discharge indicates that these values can be slightly underestimated. The central safety factor obtained in simulations with the measured electron temperature is slightly above one (dashed curve on bottom panel of Fig.11) and this value is still within the scattering of the EFIT reconstruction points. Thus, a small overestimation of the electron temperature peaking changes completely the prediction for the MHD activity in the simulated scenario from sawtooth-free to sawtoothing. It should be mentioned that the radial profile of the calculated voltage is nearly flat at the end of the NBI heating showing that the magnetic configuration in Pulse No: 70199 is close to the stationary (the radial variation of the toroidal voltage is within +/−10% at $\rho < 0.75$).

Since the simulations predict that toroidal rotation plays an important role in the stabilisation of the anomalous thermal ion transport due to its dominant contribution to the $E \times B$ rotation shear, the self-consistent modelling of momentum and thermal transport and current diffusion would be important for the projection of this scenario to a different parameter space, in particular, to a larger NBI heating. In the absence of a well validated model for momentum transport the simulations of toroidal momentum in Pulse No: 70199 have been performed assuming that the momentum diffusivity χ_φ is a fraction of the thermal ion diffusivity χ_i [30]. By performing the modelling with different χ_φ/χ_i ratio it was found that the best agreement between the momentum predicted in the self-consistent modelling and estimated in the interpretative TRANSP simulations for Pulse No: 70199 has been obtained under assumption of $\chi_\varphi = 0.4\ \chi_{i,GLF23} + \chi_{i,neocl} + \chi_{\varphi,neocl}$ (here $\chi_{i,GLF23}$ is the thermal ion diffusivity computed with the GLF23 model, $\chi_{\varphi,neocl}$ is the neoclassical momentum diffusivity, which is two orders of magnitude smaller than $0.4\ \chi_{i,GLF23}$ and $\chi_{i,neocl}$, and $\chi_{i,\,neocl}$ is the neoclassical thermal ion diffusivity). To prevent a sharp local peaking of the electron temperature in the central region $\rho \le 0.1$ when the anomalous transport is suppressed (such peaking crucially affects the q_0 evolution), the minimum of anomalous thermal electron diffusivity χ_e in this region has been arbitrary limited to $0.4 m^2/s$. Then, the temperatures, current density profile and momentum in Pulse No: 70199 have been simulated with this modified model. The profiles of electron and ion temperature, toroidal velocity, current density and safety factor obtained in these simulations are shown on Fig.12. The evolution of electron and ion temperature and safety factor simulated self-consistently with momentum balance is similar to their evolution shown on Fig.11. The magnetic configuration obtained near the end of the NBI heating is characterised by a broad bootstrap current density profile and slightly off-axis beam driven current (Fig. 12c) as in the TRANSP simulations.

Based on the satisfactory agreement of the simulated and measured parameters the modelling of this scenario has been performed in an extended parameter space. In particular, the projection of the experimental scenario to fully non-inductive steady-state operation by increasing the NBI power, applying strong electron heating and raising the density and density peaking has been investigated, assuming that the obtained magnetic equilibria will be MHD stable; the analysis of the MHD stability is important for the scenario optimisation, but it is outside the scope of the present study.

The non-inductive current obtained in the reference Pulse No: 70199 with artificially increased NBI power is shown in Fig. 13 (closed triangles on the top panel). In the modelling this NBI power has been added at 5 s and maintained until the end of the actual NBI heating using the parameters of one of the JET off-axis beams (PINI 2 in octant 4) with an energy of injected neutrals of 106keV. The artificially added power has been varied from 3 to 14MW in different simulations. Since the added neutral beam injection in this predictive modelling increases the population of fast ions above the level computed for experimental scenarios certain assumptions on the thermal species are made to assure quasi-neutrality. It has been assumed here that the deuterium and impurity density remain the same as in actual experiment on which the predictive modelling is based during the NBI power scan, while the electron density increases after 5 s to maintain quasi-neutrality as the fast ion (NBI) population increases. The effect of varying the main ion density and the density peaking will be analysed separately. As shown in Fig.13 (closed symbols) the increase of the NBI power is accompanied by a large increase of the beam driven current while the bootstrap current is only weakly affected. A weak variation of the bootstrap current with strong NBI heating can be explained by the strong "stiffness" of the temperature profiles predicted with the GLF23 model. Indeed, when the NBI power is nearly doubled (P_{NBI} = 28MW) the central electron and ion temperatures increase by only 10%, but the narrow and weak ion ITB (see Fig.12a) expands out to $\rho \approx 0.35$ and it becomes steeper (note also that the NBI heating profiles are off-axis since the off-axis beam configuration has been used for the artificial NBI power scan). The toroidal rotation velocity strongly increases with the torque (by 50% at P_{NBI} = 28MW) and this increase is important for the extension of the ion ITB. This temperature evolution combined with an increase of electron density results in a moderate increase of $\beta_{N,thermal}$ (by 24%). In contrast, the fast ion normalised pressure $\beta_{N,fast}$ increases with the NBI power from 1.08 in the reference discharge to 2.47 at P_{NBI} = 28MW, leading to the strong increase of the total β_N (Fig.13, bottom). The ratio of the thermal to the total normalised pressure strongly reduces over the power scan under assumption of fixed ion density (from 0.67 in Pulse No: 70199 to 0.53 with 28MW of NBI). The full non-inductive current has been obtained at $\beta_N \approx 5.2$ in these simulations (compare to Fig.5, top) when the beam driven current achieves 64% of the total current. The current density profiles obtained close to fully non-inductive operation are shown in Fig.14, together with the safety factor and toroidal voltage profiles. A weakly reversed q-profile in the plasma core has been obtained with $q_{min} > 1$.

Keeping in mind that the electron temperature gradient produces the largest contribution to the bootstrap current in this scenario (Fig.6) an attempt to increase the bootstrap current by applying strong electron heating (e.g., Ion Cyclotron heating) has been performed. The strong electron heating with power up to 15MW and slightly off-axis Gaussian deposition profile (with a maximum located at $\rho = 0.1$ and a width $\Delta\rho = 0.25$) has been applied at 5s on the top of the actual NBI heating. These simulations have been performed with the measured toroidal rotation. The non-inductive current and normalised pressure achieved with strong electron heating are added in Fig.13 (open symbols) for the comparison with the NBI power scan. It has been found that the electron temperature increases by a factor 2 reaching 9.5keV when 15 MW of electron heating is applied. However, such a strong increase

of T_e is accompanied by a large reduction of the ion temperature (by 40%) which is due to the destabilising effect of the T_e /T_i ratio on the ITG turbulence as demonstrated in Ref. 16. A similar effect has been obtained in the comparative simulations of JET regimes with strong ion heating and strong electron heating with the Weiland model [31], where an increased electron heating deteriorated the confinement. The reduction of T_i in the present simulations restricts the increase of thermal and total β_N with electron heating leading to lower β_N values when the same total heating power (i.e. the sum of electron heating and NBI power), as in the pure NBI heating case, is applied (Fig.13, bottom). As a result, the increase of the bootstrap current and total non-inductive current with electron heating power is not large.

The evolution of the non-inductive current with plasma density at constant NBI power is illustrated in Fig.15. In these simulations the deuterium and impurity density profiles have been rescaled after 5s by the same factor to maintain a nearly unchanged Z_{eff} during the density scan. The electron density has been estimated from the quasi-neutrality equation taking into account the simulated fast ion density. As shown in Fig. 15 the density increase is highly beneficial for the bootstrap current. However, the total non-inductive current weakly varies with density since the increase of the bootstrap current is compensated by the nearly equal reduction of the beam driven current due to its inverse density-dependent current drive efficiency.

In the plasmas analysed in this paper the density peaking varies from 1.2 to 1.6 (see Refs. 32 and 33 for density peaking at JET). Pulse No: 70199, taken as a reference for predictive modelling, is characterised by a moderate density peaking $n_{e0}/<n_e> \approx 1.45$ (Fig.16), which is typical for many analysed discharges. However, in some cases a higher density peaking has been achieved (for example in Pulse No: 68876, Fig. 16) that should be beneficial for the bootstrap current. The effect of the density peaking on the non-inductive current drive has been estimated by repeating the NBI power scan, similar to one shown on Fig.13, for plasma with highest density peaking. The same reference Pulse No: (70199) where the original density has been replaced after 5s by the density profile with the highest peaking (taken from Pulse No: 68876, Fig.16) has been used for these simulations. This peaked density profile has been kept constant until the end of the NBI heating (t = 11s). The simulations show little effect of the peaked density profile on the total non-inductive current. Indeed, the bootstrap current increases with density peaking, but the NBI current drive efficiency for the beams deposited close to the plasma centre drops with the peaked density profile. Thus, the increased bootstrap current is compensated by the reduced beam driven current resulting in a weak dependence of the total non-inductive current on density peaking at various NBI powers. As a result, full non-inductive current drive is achieved at about the same total NBI power P_{NBI} = 28MW in plasmas with high ($n_{e0}/<n_e>$ = 1.6) and low ($n_{e0}/<n_e>$ = 1.2) density peaking.

SUMMARY AND DISCUSSION

The transport and non-inductive current drive in JET plasmas, characterised by high β_N values (up to 3.3) without a strong ITB, has been analysed here by using the TRANSP and ASTRA codes. The

results of the interpretative analysis of the current drive and the q-profile evolution performed with the TRANSP code can be summarised as follows:

- non-inductive current up to 75% (0.9MA) has been achieved before the onset of an $n = 1$ mode in discharges with high NBI power (20–22MW), but this current can be strongly reduced by the MHD modes. A non-inductive current drive fraction close to 60% has been maintained in stationary conditions at a lower power throughout the NBI heating phase. The total non-inductive current is composed of nearly equal bootstrap and beam driven currents. It should be noted that the fast ion current drive is computed under the assumption of classical diffusion of fast ions;
- the current density profile is composed of a broad bootstrap and slightly off-axis beam driven current density profiles in the majority of discharges. The remaining ohmic current is nearly relaxed in discharges with long NBI heating;
- the electron temperature gradient provides the dominant contribution to the total bootstrap current for the majority of discharges. The low peaking of the density profile is a reason for the smaller contribution of the density gradient to the bootstrap current;
- a monotonic q-profile with q_0 slightly above one has been maintained until the end of the high power heating phase (for 7–8s) in the MHD stable discharges with moderate NBI power (~14–17MW).

Predictive modelling of thermal transport for 12 discharges with different NBI start times, heating powers and current ramp rates performed with the GLF23 model in the ASTRA code shows a reasonable predictive capability of this model (the discrepancy between measured and simulated temperatures is within +/–22%). The comparison of the simulated ion temperature with the GLF23 model in ASTRA and TRANSP for two discharges demonstrated a good agreement between these codes. The $E \times B$ rotation shear is predicted to play an important role in these discharges, reducing the ITG driven thermal ion transport and providing up to a 40% increase of the core ion temperature. The toroidal rotation shear produces the dominant contribution to the $E \times B$ rotation shear under the assumption that the poloidal rotation is neoclassical.

The measured electron temperature profiles are generally broader than the simulated profiles, although the central electron temperature is reasonably well predicted. However, even a small overestimation of the electron temperature peaking produces an important effect on the evolution of the central q and on the prediction for the sawtooth activity in this scenario. This result should be kept in mind when applying these models to ITER scenarios. Previous simulations of the ITER scenario with the plasma current varying in the range 9–13MA performed with the same models show that the q_0 value drops to one within the first 120s of the discharge [34]. The sensitivity of this result to the electron temperature peaking still remains to be investigated. It should be mentioned that a flattening of electron temperature profile can be caused by moderate MHD activity (small sawteeth or fishbones), which in this case produces a beneficial effect on the stationary magnetic equilibrium by maintaining q_0 above one.

The transport and current drive models validated in self-consistent simulations of the thermal energy and momentum balance and current profile diffusion, for the reference discharge with a long NBI heating phase, have been applied for the projection of high β_N plasmas towards an extended

parameter space to estimate the requirements of fully non-inductive operation at JET, and test the sensitivity to the heating and density rise. It was found by increasing the plasma heating that the strong "stiffness" of the temperature profiles obtained with the GLF23 transport model is an important limiting factor for the bootstrap current. The density rise performed both by rescaling the moderately flat profile and by increasing the density peaking produces a beneficial effect on the bootstrap current, but the inverse dependence of the NBI current drive efficiency on the plasma density leads to the reduction of the beam driven current. As a result, the only fully non-inductive solution found in the predictive simulations required a strong increase of the NBI power. It should be mentioned that Lower Hybrid Current Drive (LHCD) is also available on JET to help reaching non-inductive operation, but an increase in magnetic field would be needed since LH waves can not access the region of interest at the low magnetic field and high density considered.

The extrapolation of the dependence of the total non-inductive current on β_N towards fully non-inductive operation (Figs. 5 and 13) shows that full non-inductive current drive might be obtained at β_N close to 5 for the conditions considered (although this estimation may be lower if the pressure gradient in the pedestal region is underestimated with the assumptions made in TRANSP). This β_N value exceeds the empirical $4l_i$ limit, but detailed stability calculations are beyond the scope of this paper. The experiments show that the plasma performance at larger NBI power is limited by MHD modes. The predictive modelling of the thermal balance and current diffusion, in combination with an MHD stability analysis of the transient plasma states and the steady-state magnetic equilibrium with high β_N is required for the further development of this scenario towards fully non-inductive MHD stable operation. Also consideration should be given to means to improve the thermal confinement, such as ITBs or hybrid regime operation.

ACKNOWLEDGEMENTS

Drs. T. C. Hender, W. Morris, V. Pericoli-Ridolfini, F. Rimini, T. Tala and R. Kamendje are warmly acknowledged for useful comments leading to improvements in the manuscript. This work was partly funded by the United Kingdom Engineering and Physical Sciences Research Council and by the European Communities under the contract of Associations between EURATOM and UKAEA. The views and opinions expressed herein do not necessarily reflect those of the European Commission. This work has been carried out within the framework of the European Fusion Development Agreement. The contribution of the US co-authors to this work is supported by the US DoE contracts Nos DE-AC02-76CH03073 and E-FG02-07ER54927.

REFERENCES

[1]. K.H. Burrell and the DIII-D Team, Nucl. Fusion **43** (2003) 1555
[2]. T.C. Luce and the DIII-D Team, Nucl. Fusion **45** (2005) S86
[3]. M. Murakami, C M Greenfield, M R Wade *et al*, Nucl. Fusion **45** (2005) 1419
[4]. H. Takenaga and the JT-60 Team, Nucl. Fusion **47** (2007) S563

[5]. S. Ide and the JT-60 Team, Nucl. Fusion **45** (2005) S48
[6]. A.C.C. Sips, R .Arslanbekov, C. Atanasiu *et al*, Plasma Phys. Contr. Fusion **44** (2002) B69
[7]. M.A. Henderson, S. Alberti, C. Angioni *et al,* Phys. Plasmas **10** (2003) 1796
[8]. I. Voitsekhovitch, D. Moreau, Nucl. Fusion **41** (2001) 845
[9]. D. Moreau, I. Voitsekhovitch, Nucl. Fusion **39** (1999) 685
[10]. D. Moreau, F. Crisanti, X. Litaudon *et al*, Nucl. Fusion, **43** (2003) 870
[11]. M. Shimada, D.J. Campbell, V. Mukhovatov *et al*, Nucl. Fusion **47** (2007), S1
[12]. C.D. Challis, E. Joffrin, T Luce *et al*, 34rd EPS Conference on Plasma Phys., Warsaw, 2-6 July 2007, in press
[13]. V. Pericoli-Ridolfini, Yu Baranov, M Beurskens *et al*, 35th EPS Conference on Plasma Phys., Hersonissos, Greece, 9-13 June 2008, in press
[14]. R.J. Goldston, D.C. McCune, H.H. Towner, S.L. Davis, R.J. Hawryluk and G.L. Schmidt, J. Comp. Physics **43** (1981) 61
[15]. G.V. Pereverzev, P N Yushmanov, Report IPP 5/98, Max-Planck-Institute fur Plasmaphysik, 2002
[16]. R.E. Waltz, G.M. Staebler, W. Dorland, G.W.Hammett, M. Kotschenreuther, and J.A. Konings, Phys. Plasmas **4** (1997) 2482
[17]. P. Buratti, C D Challis, M Gryaznevich *et al*, 35th EPS Conference on Plasma Phys., Hersonissos, Greece, 9-13 June 2008, in press
[18]. D.P. O'Brien, L L Lao, E R Solano *et al*, Nucl. Fusion **30** (1992) 1351
[19]. C.D. Challis, J G Cordey, H Hamnen *et al*, Nucl. Fusion **29** (1989) 563
[20]. S.E. Sharapov, B Alper, H L Berk *et al*, Phys. Plasmas **9** (2002) 2027
[21]. W.A. Houlberg, K.C. Shaing, S.P. Hirshman, M.C Zarnstorff, Phys. Plasmas **4** (1997) 3230
[22]. A. Pankin, D McCune, R. Andre, G. Bateman, A. Kritz, Comp. Phys. Comm. **159** (2004) 157
[23]. J.R. Ferron, V Basiuk, T.A. Casper *et al*, Proceedings of 21st IAEA Conference, Chengdu, 16–21 October 2006, paper EXP/P1-4.
[24]. O. Sauter, C. Angioni, Y.R. Lin-Liu, Phys. Plasmas **6** (1999) 2834
[25]. Y.I. Kolesnichenko, V.V. Parail, G.V. Pereverzev, Reviews of Plasma Phys. **17** (1992) 1
[26]. C Giroud, A.G. Meigs, C.R. Negus *et al*, Proceedings of the 17th Topical Cong. On High Temperature Plasma Diagnostics, Albuquerque, New Mexico, May 2008, submitted to Rev. Scien. Instrum.
[27]. K. Crombe, Y. Andrew, C Giroud *et al*, Phys. Rev. Lett., **95** (2005), 155003
[28]. J.E. Kinsey, G.M. Staebler and R E Waltz, Phys. Plasmas **9** (2002) 1676
[29]. A. Polevoi, H Shirai, T Takizuka, Report JAERI-Data/Code 97-014, March 1997
[30]. P.C. de Vries, K.M. Rantamaki, C. Giroud *et al,* Plasma Phys. Contr. Fusion **48** (2006) 1693
[31]. J. Weiland, E .Asp, X Garbet *et al,* Plasma Phys. Contr. Fusion **47** (2005) 441
[32]. M. Valovic, L.Garzotti, I. Voitsekhovitch *et al*, Nucl. Fusion **47** (2007) 196
[33]. H. Weisen, A. Zabolotsky, M. Maslov *et al*, Plasma Phys. Contr. Fusion **48** (2006) A457
[34]. I. Voitsekhovitch, B. Alper, M Brix *et al,* 49th Annual Meeting of the Division of Plasma Physics, Orlando, 2007.

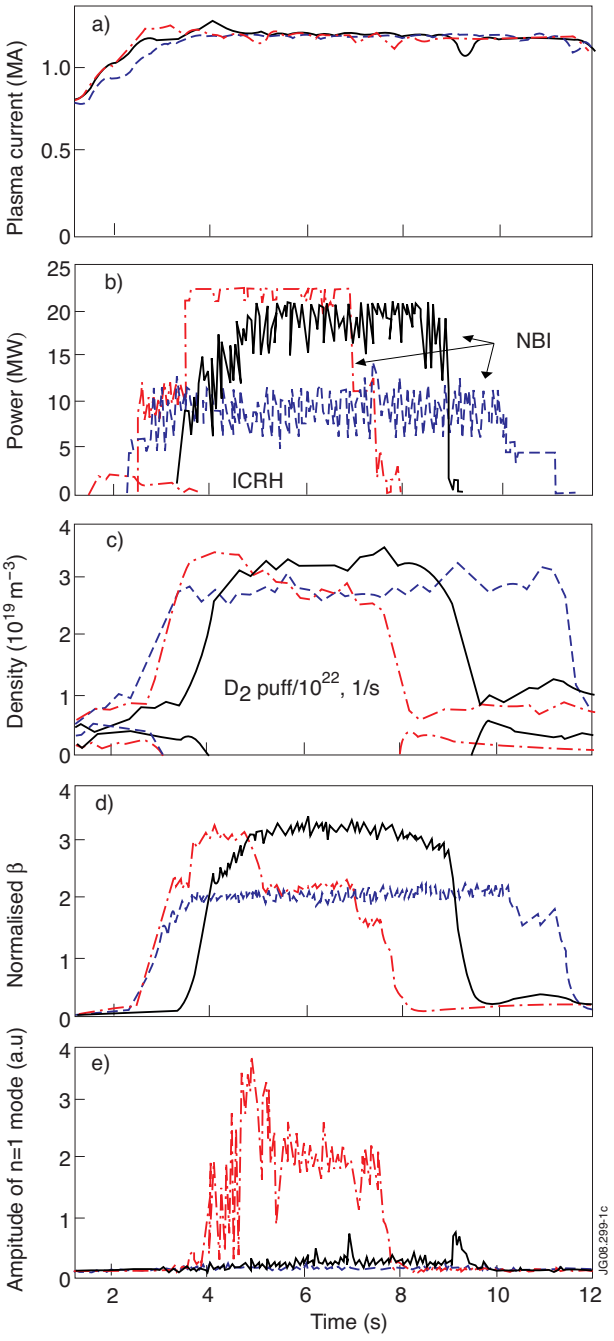

Figure 1: Typical high β_N scenario: plasma current (a), NBI and ICRH power (b); line averaged density (c), diamagnetic β_N (d) and the amplitude of n = 1 mode measured by toroidally separated sensors (e) for Pulse No's: 68767 (dashed-dotted curves), 68875 (solid curves) and 70207 (dashed curves). ICRH power in Pulse No: 68767 is shown by dashed-dotted curve in second panel.

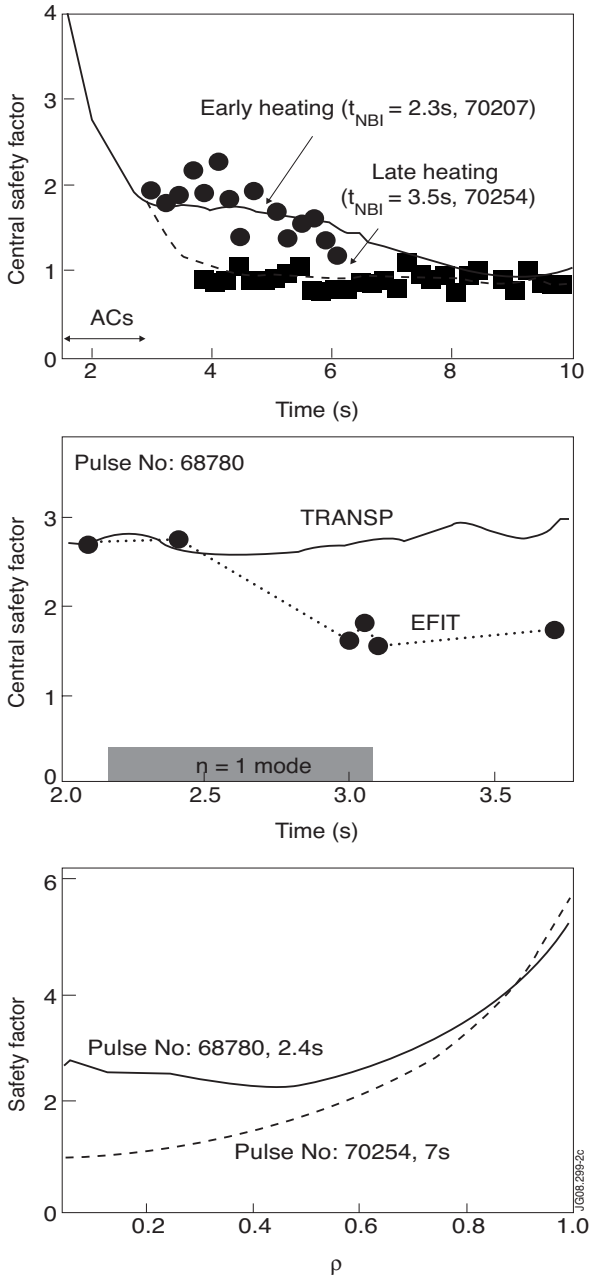

Figure 2: Top: evolution of the central safety factor in Pulse No's: with early (70207) and late (70254) heating. Middle: evolution of the central safety factor in discharge with earliest NBI heating and largest current ramp rate (Pulse No: 68780) where the ACs have been observed during the whole NBI heating phase (see Session III). Curves on the top and middle panels show the TRANSP simulations, symbols correspond to the EFIT reconstruction. Bottom: typical weakly reversed safety factor profile obtained at early phase during the current ramp up (68780, 2.4s) (solid curve) and typical monotonic profile obtained at the end of high power phase (Pulse No: 70254, 7s) (dashed curve).

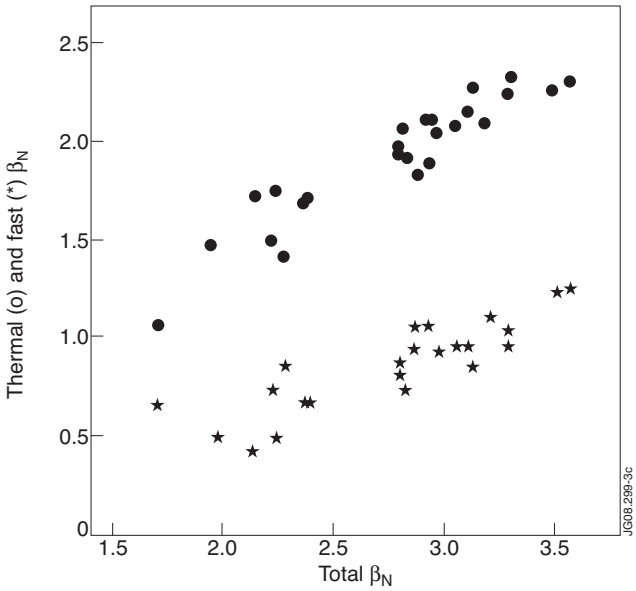

Figure 3: Thermal (circles) and fast ion (asterisks) β_N plotted as a function of total β_N computed in TRANSP for 26 discharges. The data are averaged over 0.3s before the onset of n = 1 mode or during the stationary phase in the MHD stable discharges. The deviation of the total β_N calculated by TRANSP from the diamagnetic β_N is within 7%.

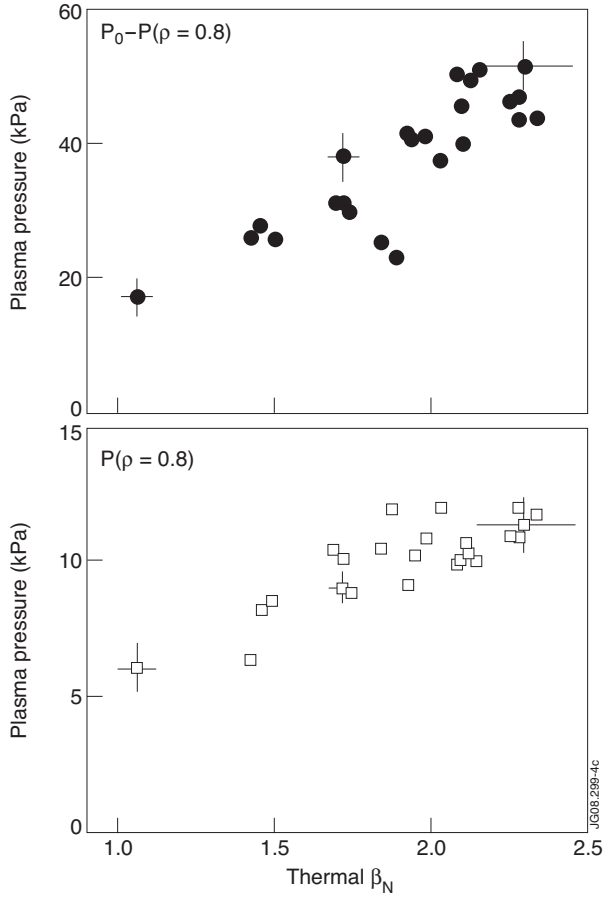

Figure 4: Difference between the central pressure P_0 and pressure at ρ = 0.8 (top) and the pressure at ρ = 0.8 (bottom) as a function of thermal β_N. The same time interval for averaging as on Fig.3 is used. Error bars are determined by the temporal variation of plotted parameters during the time interval used for averaging.

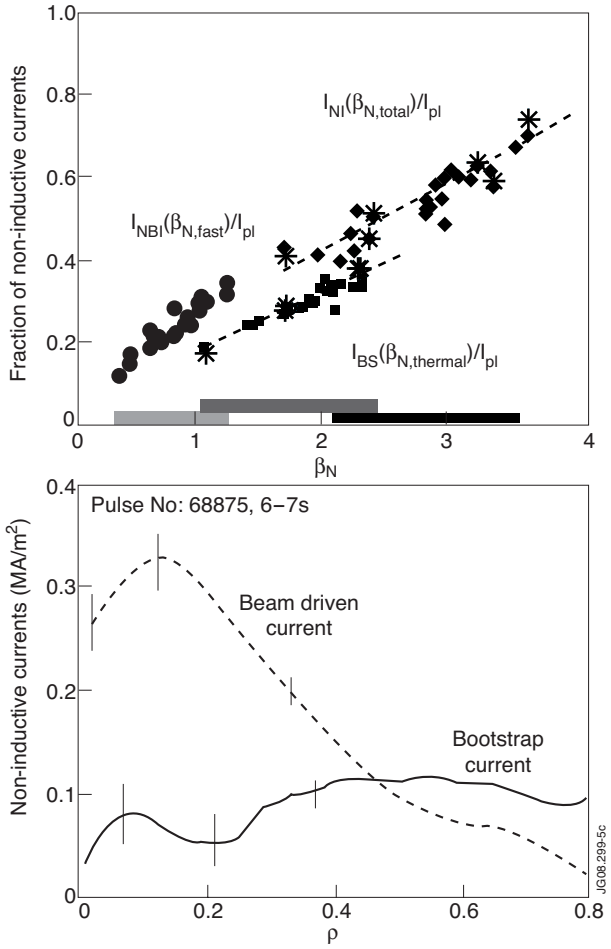

Figure 5: Top: beam driven current, $I_{NBI}(\beta_{N,fast})$, bootstrap current, $I_{BS}(\beta_{N,thermal})$, and total non-inductive current, I_{NI} ($\beta_{N,tot}$) = I_{NBI} + I_{BS}, are respectively plotted as function of fast ion $\beta_{N,fast}$ (circles), of thermal $\beta_{N,thermal}$ (squares) and of total $\beta_{N,tot}$ (diamonds). The intervals of the horizontal axis indicating the range of $\beta_{N,fast}$, of $\beta_{N,thermal}$ and of $\beta_{N,tot}$ are shown by light grey, dark grey and black respectively. The currents are simulated with NCLASS, except those represented by asterisks that are derived from the Sauter model. The same time interval as on Fig.3 is used for averaging. Bottom: typical profile of the beam driven current and bootstrap current achieved in JET high β_N scenario (68875). Error bars are determined by the variation of these profiles during 1s.

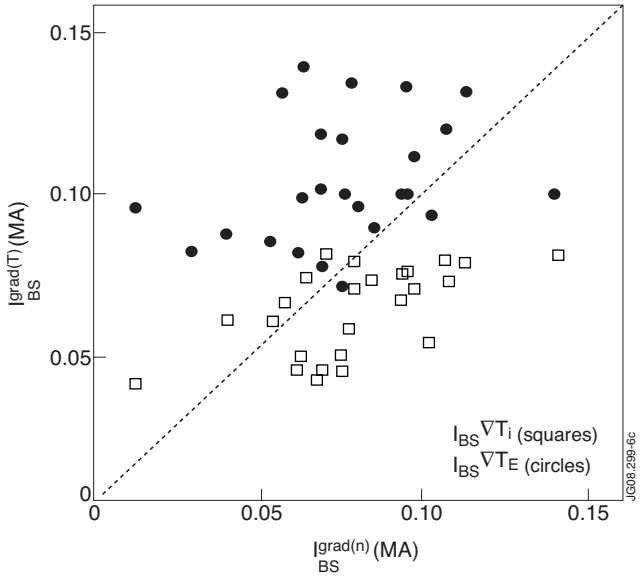

Figure 6: The bootstrap current term driven by ∇T_e (circles) and ∇T_i (squares) as a function of the bootstrap current term driven by ∇n for 26 discharges. The same time interval for averaging as on Fig. 3 is used. Dashed line corresponds to the condition $I_{BS}^{\nabla T} = I_{BS}^{\nabla n}$.

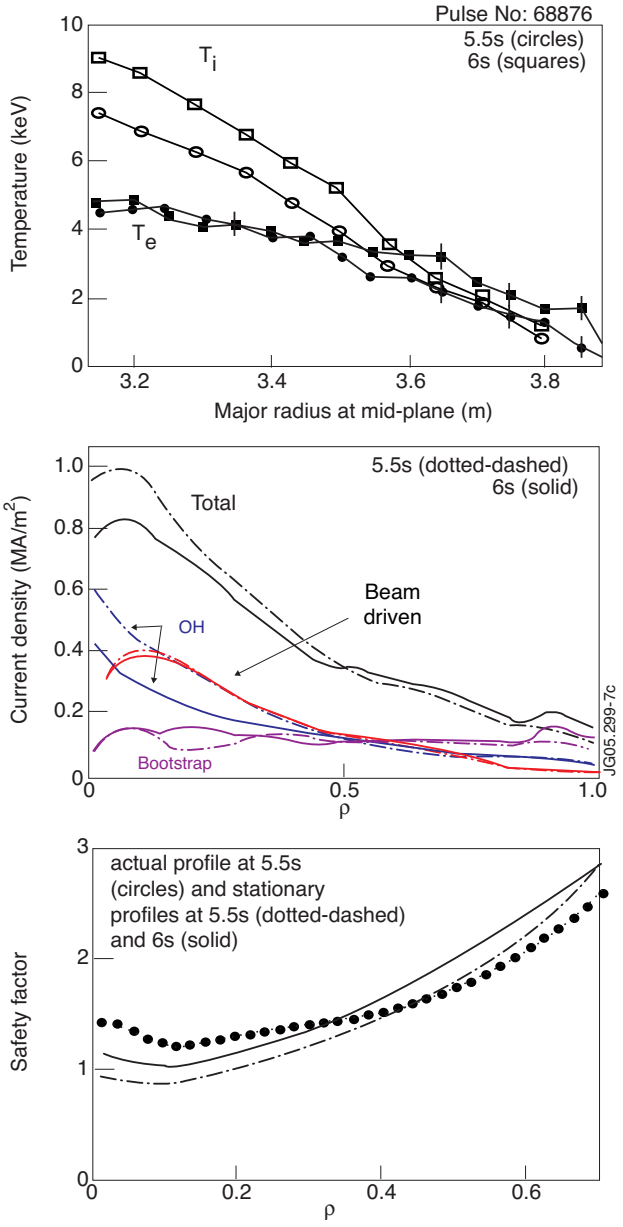

Figure 7: Top: measured ion (open symbols) temperature at 5.5 (circles) and 6s (squares) in discharge 68876. Electron temperature shown for the same times is obtained by averaging the measured temperature at 5.3871s and 5.6281s, and 5.8782s and 6.1282s correspondingly. The error bars on electron temperature show the deviation from measured values. The error bars on ion temperature are within 2%. Middle: steady state total, beam driven, bootstrap and ohmic current density profiles obtained by freezing the plasma profiles at 5.5s (dotted-dashed curves) and 6s (solid curves). Bottom: actual safety factor profile at 5.5s (circles) and stationary q*-profiles obtained by freezing the plasma profiles at 5.5s (dotted-dashed curves) and 6s (solid curves).*

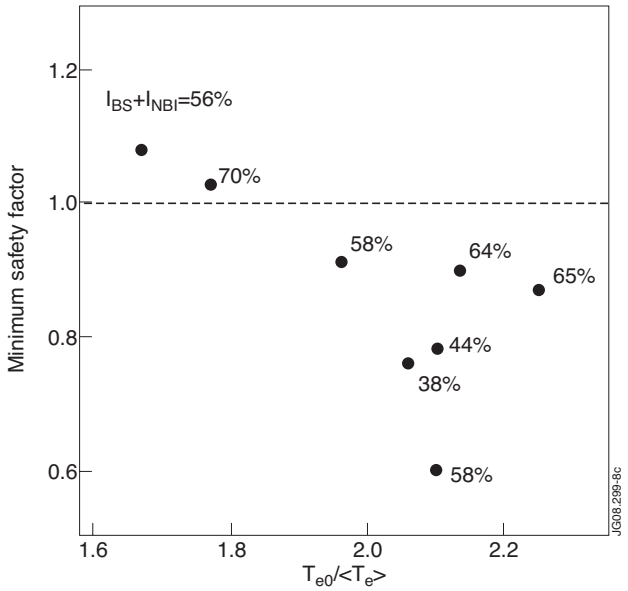

Figure 8: Steady-state minimum (or central for the cases with monotonic q) safety factors, obtained in predictive modelling with TRANSP by freezing the plasma profiles and NBI power at a given time, plotted as a function of electron temperature peaking. The total non-inductive current is indicated for each simulation. The simulations are performed for discharges 69001 (profiles are frozen at 5.52s), 68767 (profiles are frozen at 4.4 and 6.2s), 68876 (profiles are frozen at 5.5 and 6s) and 70199 (profiles are frozen at 7.09 s).

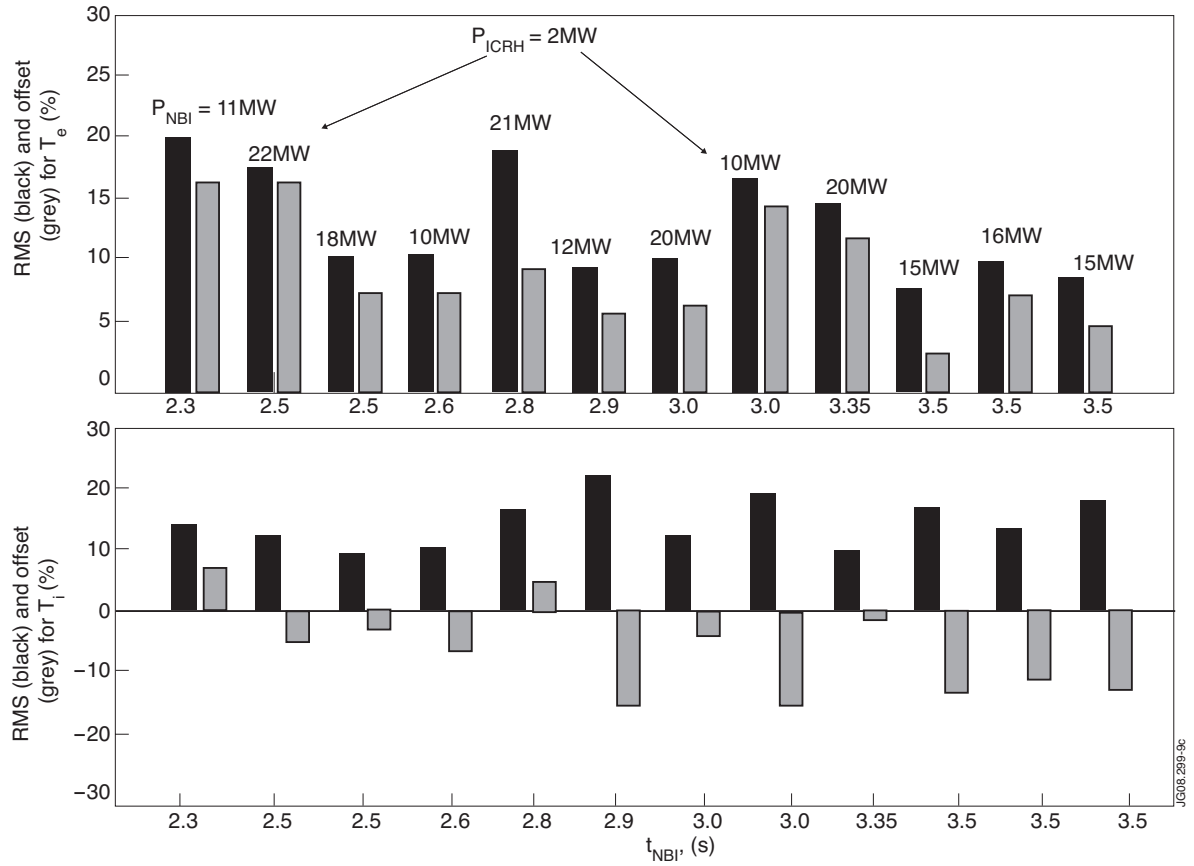

Figure 9: RMS deviation (black bars) and offset (grey bars) obtained for the electron (top) and ion (bottom) temperature simulated with the GLF23 model for discharges with different NBI start time and heating power. The NBI start time is indicated on the bottom of each panel and the applied maximum NBI power is indicated near each bar on the top panel. Two discharges with 2MW of ICRH power are shown by arrows on the top panel.

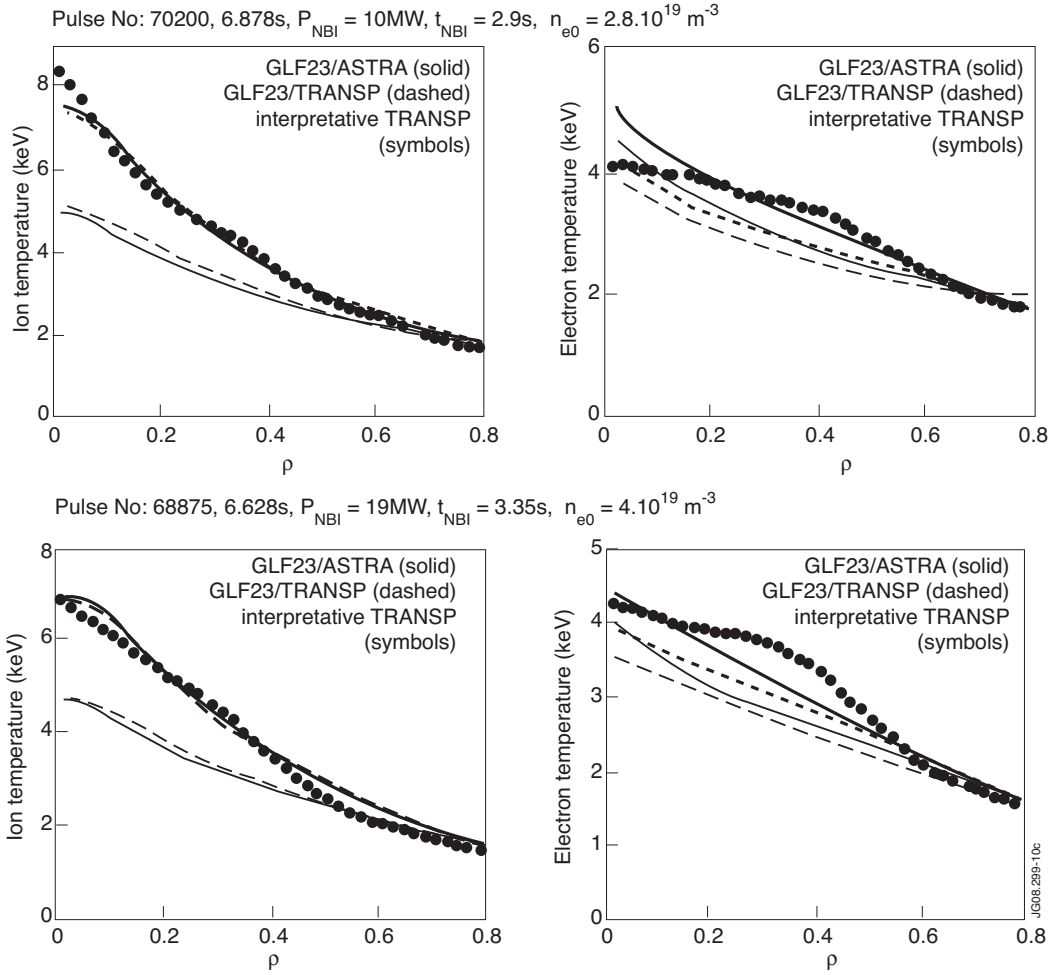

Figure 10: Ion (left column) and electron (right column) temperature profiles simulated by using the GLF23 model in ASTRA (solid curves) and TRANSP (dashed curves) in discharge with low electron density and NBI power (top panels) and high electron density and NBI power (bottom panel). The simulations with and without the E×B shear in the GLF23 model are shown by bold and thin curves correspondingly. Symbols show the profiles from interpretative TRANSP simulations where the experimental data are mapped to the magnetic surface computed by TRANSP.

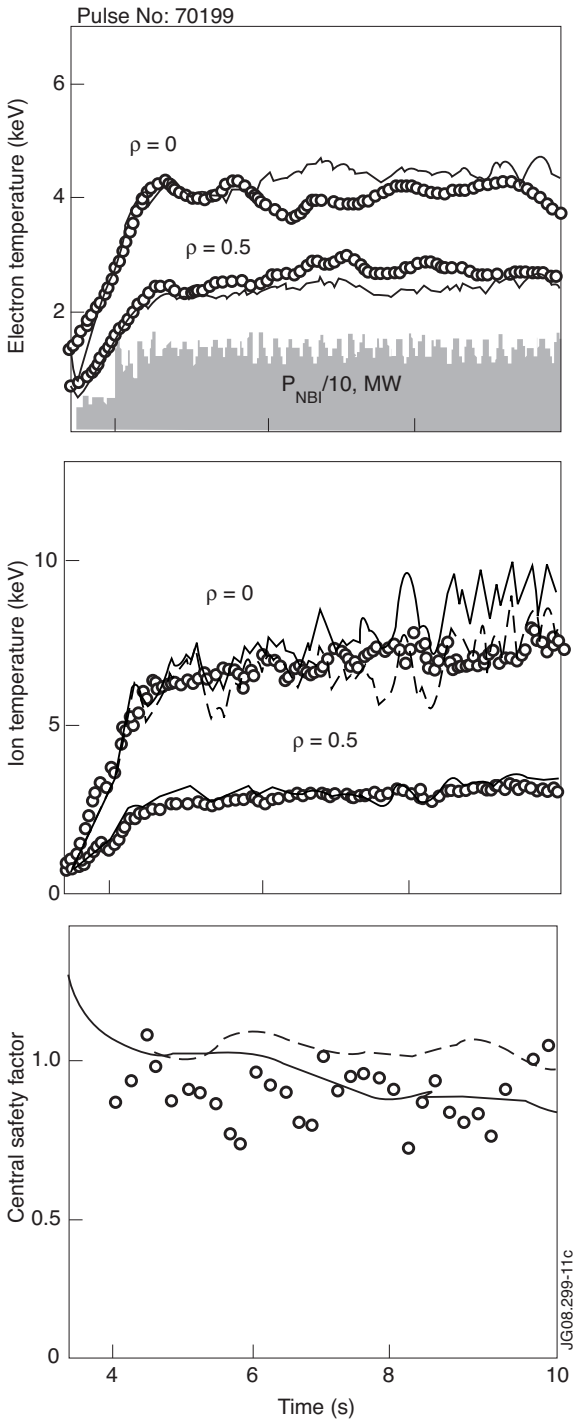

Figure 11: Electron temperature (top), ion temperature (middle) and central safety factor (bottom) obtained in the self-consistent simulations of T_e, T_i and current diffusion (solid curves) and in simulations of T_i and current diffusion with measured T_e (dashed curves). Symbols on the top and middle panels show the evolution of temperatures obtained in the interpretative TRANSP simulations with measured data. Circles on the bottom panel show the central safety factor obtained with EFIT.

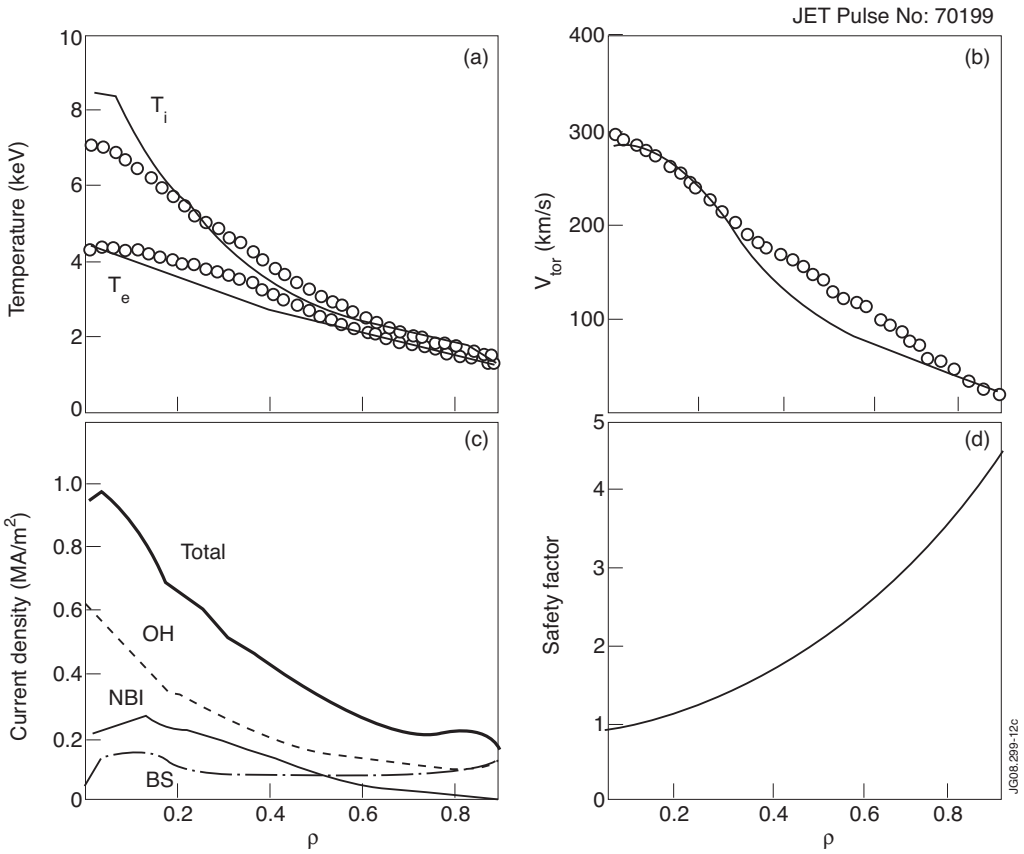

Figure 12: Electron and ion temperature (a), toroidal rotation (b), current density (c) and safety factor (d) obtained at 10s in the self-consistent simulations of energy and momentum balance and current profile diffusion of Pulse No: 70199 (curves). Symbols on panels (a) and (b) show the measured temperatures and deuterium rotation. Deuterium rotation was calculated with NCLASS in TRANSP. Panel (c) shows the total current density profile (bold solid curve), beam driven current (thin solid curve), bootstrap current (dotted-dashed curve) and ohmic current (dashed curve).

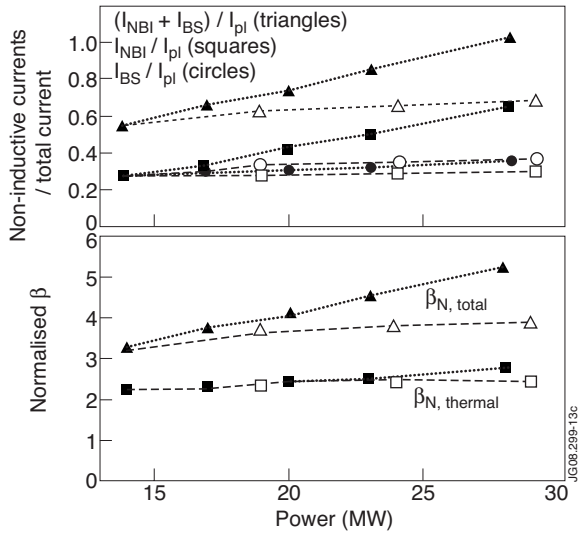

Figure 13: Top: fraction of beam driven current (squares), bootstrap current (circles) and total non-inductive current (triangles) obtained in predictive simulations based on Pulse No: 70199 where the NBI power has been artificially increased above 14MW applied in experiment (closed symbols). Open symbols show the fractions of non-inductive currents obtained in the simulations of Pulse No: 70199 where the artificial electron heating has been added. Bottom: total (triangles) and thermal (squares) β_N obtained by varying the artificially added NBI power (closed symbols) and electron heating power (open symbols). Horizontal axis on both panels represents the total heating power (NBI power only for the P_{NBI} scan or the sum of the NBI and electron heating powers for the electron heating power scan). All parameters are averaged over the time interval 9–10s.

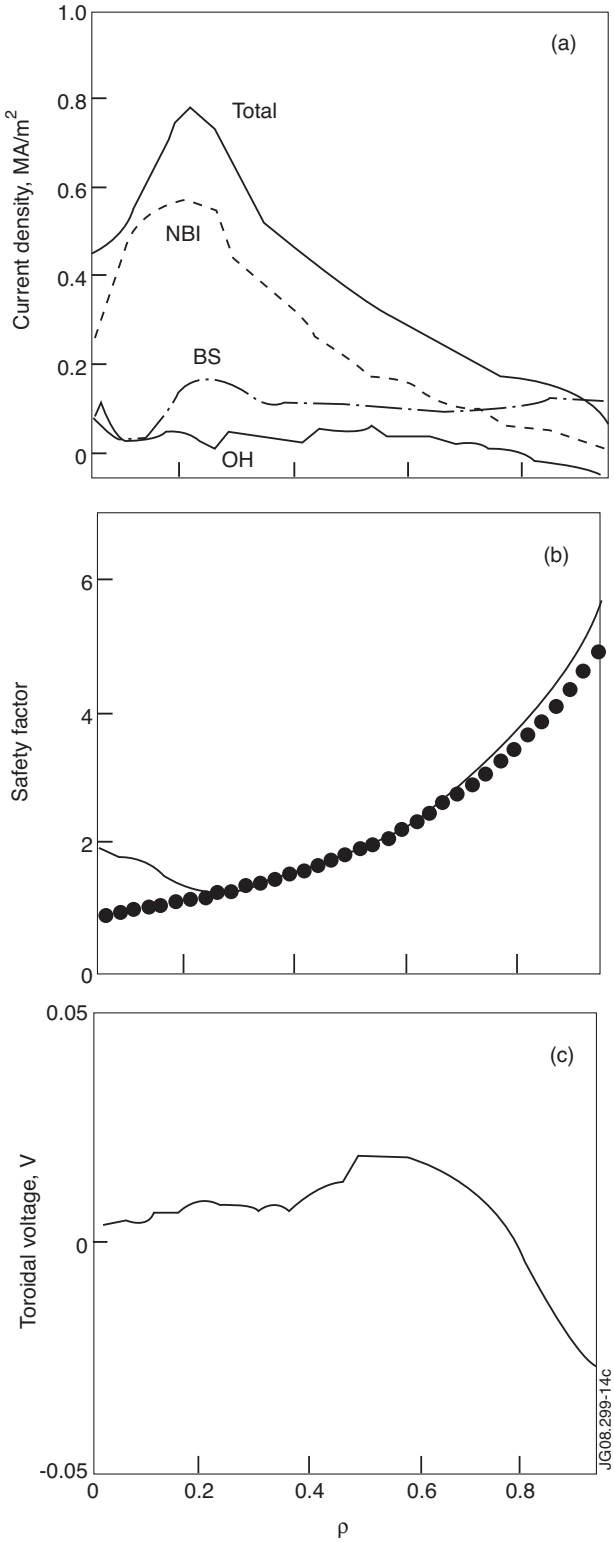

Figure 14: Total (bold solid curve), beam driven (dashed curve), bootstrap (dotted-dashed curve) and ohmic (thin solid curve) current density profiles (a), safety factor (solid curve) (b) and toroidal voltage (c) profiles obtained at 10s in simulations with artificially increased NBI power in discharge 70199 (P_{NBI} = 28MW). Symbols on the middle panel show the safety factor profile obtained at 10s in Pulse No: 70199.

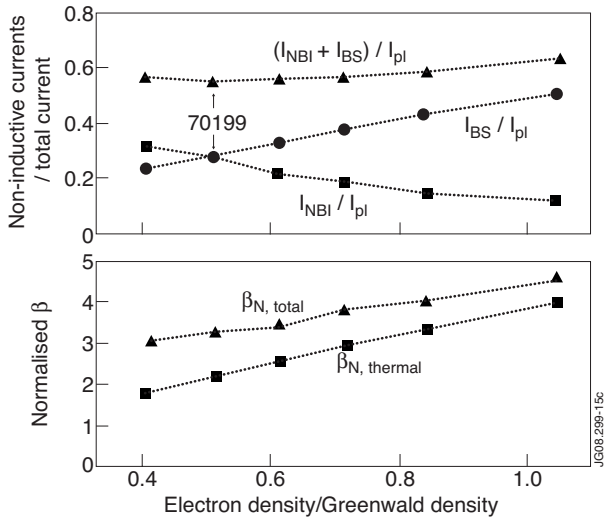

Figure 15: Fractions of the non-inductive currents (top) and normalised β_N (bottom) obtained in the simulations based on Pulse No: 70199 where the plasma density was artificially varied. Triangles on the top panel show the total non-inductive current fraction, squares show the beam driven current fraction and circles show the bootstrap current fraction. Triangles and squares on the bottom figure show the total and thermal β_N correspondingly. All parameters are averaged over the time interval 9–10s.

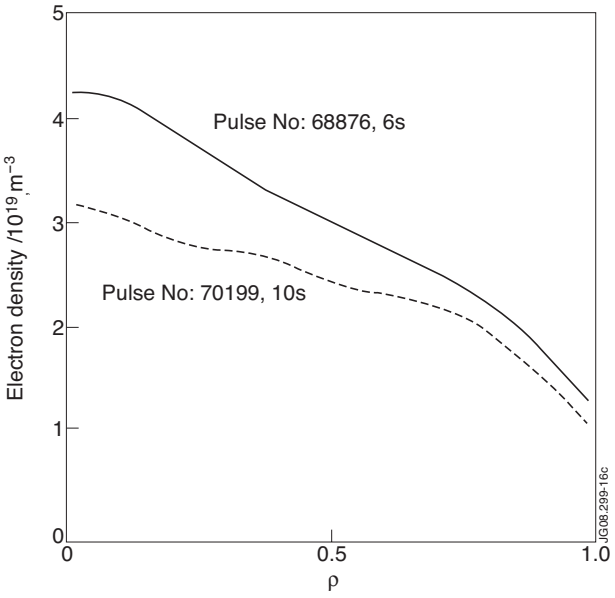

Figure 16: Density profile in Pulse No's: 70199 at 10s and 68876 at 6s illustrating the typical and largest density peaking achieved in high β_N scenario.